ADVANCED STUDY OF SECONDARY FLOW STRUCTURES IN A HIGHLY LOADED COMPRESSOR CASCADE

A. Hergt, J. Klinner, C. Morsbach, M. Franke, S. Grund

German Aerospace Center (DLR)
Institute of Propulsion Technology
Linder Hoehe, 51147 Cologne, Germany
alexander.hergt@dlr.de

ABSTRACT

The current paper deals with a detailed experimental and numerical investigation of the secondary flow structures in the corner region between blade and endwall in a highly loaded compressor cascade, with the objective to provide extensive validation data and performing a first comparison with numerical results. The used cascade has been designed and optimized specifically for use at low Reynolds number conditions, as can be found at high altitudes. The study was divided into an experimental and a numerical part. The experimental part of the investigation was performed in the transonic cascade wind tunnel of DLR in Cologne at a Mach number of 0.6 and Reynolds number of 9.0x10^5. Wake measurements with a 5-hole probe at four distances behind the cascade trailing edge were carried out, in order to obtain measurement data of the loss distribution, comparable to the numerical results. Furthermore, oil streak patterns on the endwall and blade surface were conducted. Additionally, tomographic PIV (tomo-PIV) and conventional stereo PIV (SPIV) are utilized, in order to assess the quality of CFD prediction of the flow structure in the corner region.

The numerical investigation of the cascade flow was performed by means of the turbomachinery CFD code TRACE, which is an in-house developed code of the DLR Institute of Propulsion Technology. The focus was on the detailed description of the secondary flow close to the corner region and on the determination of the loss distribution in the wake behind the cascade. Furthermore, the influence of the boundary layer transition on the cascade flow was considered by the usage of a transition model.

In the paper a detailed comparison between the experimental and the nurmerical results is given. It is shown, that the experimental extension of the corner separation on the cascade surfaces and the development of the loss distribution behind the cascade is well reflected by the CFD results, but there are differences in the loss intensity.

NOMENCLATURE

+ Latin

AVDR	axial velocity density ratio = $\frac{\rho_2 \cdot v_2 sin\beta_2}{\rho_1 \cdot v_1 sin\beta_1}$	mag_{vw}	magnitude v-w velocity vectors
c	profile chord length	p	pressure
d	distance from trailing edge	Re	Reynolds number based on c
h	blade span	t	pitch
i	incidence angle = $\beta_1 - \beta_{1,Design}$	u,v,w	velocity components
M	Mach number	v	velocity
x,y,z	cartesian coordinates		

Greek

β	flow angle with respect to cascade front	$\Delta\beta$	cascade deflection angle = β_1-β_2
ω	total pressure loss coefficient = $\frac{p_{t,1}-p_{t,2}}{p_{t,1}-p_1}$		

Subscripts

0	reference state
1	inlet plane
2	exit plane
ax	axial
is	isentropic
LE	leading edge
PS	pressure side
s	stagger
SS	suction side
t	total, stagnation value
TE	trailing edge

Abbreviations

ADP	aerodynamic design point
FOV	field of view
FWHM	light sheet thickness
LE	leading edge
LRN	low Reynolds number
MP1	measurement plane 1 (inlet)
MP2	measurement plane 2 (exit)
OGV	outlet guide vane
PIV	particle image velocimetry
ROI	region of interest
TE	trailing edge

INTRODUCTION

Nowadays, modern axial compressors have already reached a very high development level. In order to achieve further improvement in compressor efficiency and an accurate detection of the working range during the design process, the usage of precise numerical methods is necessary. Therefore, the development and validation of these numerical methods and the included turbulence and transition models is an important field of research. The requirements on the turbulence as well as the transition models in a turbomachinery CFD code are very high, due to the very complex three dimensional flow field in a compressor blade row [3, 5, 7, 8, 18] and the appearance of anisotropic stresses, particularly in the corner region between endwalls and blade suction side. Thus the requirements on an experimental setup and the used measurement techniques for CFD validation are also very high.

Therefore in the current study, extensive experiments were performed and their results were used for the comparison with numerical simulations. In order to provide detailed experimental data for the validation process conventional pressure probe based measurements on the cascade surfaces as well as in the wake are performed. In addition to that, optical measurement techniques are used in order to achieve the best resolution of the structure and dimension of the separated areas within the cascade. Therefore volume resolving thick-sheet PIV (or tomo-PIV) [2] and Stereo PIV [15] are applied near the trailing edge of the cascade blades. With these methods the three dimensional and time averaged velocities in the separated flow region can be obtained. Furthermore, oil streak patterns are used as a conventional method to visualize the flow structure on the cascade surfaces.

For the numerical investigation the turbomachinery CFD code TRACE [1], which is an in-house developed code of the DLR Institut of Propulsion Technology was used. The results of the numerical part of this paper present the status quo of turbomachinery simulations. They should be the basis for further validation studies using turbulence models which take anisotropy into account.

EXPERIMENTAL AND NUMERICAL SETUP

Cascade Configuration

For the experimental and numerical investigation within the study the DLR LRN-OGV cascade was used. The design and performance of this cascade is already described by Hergt et al. [4, 6]. The cascade consists of 7 blades with 70 mm chord and 168 mm blade span. Figure 1 shows the cascade which was used in the experiments. This cascade enables tests at realistic flow conditions, e.g. Mach number, thus the transferability to real turbomachines is given to a certain extent. The general design parameters of the cascade and test conditions are also shown in Fig. 1.

Inlet Mach number	M_1	= 0.60
Reynolds number	Re	= 9.0 x 10^5
Inlet flow angle at ADP	β_1	= 133.0 deg
Flow turning at ADP	$\Delta\beta$	= 43.0 deg
Stagger angle	β_{st}	= 106.4 deg
Blade chord	c	= 70 mm
Pitch to chord ratio	t/c	= 0.577
Blade span	h	= 168 mm
Blade aspect ratio	h/c	= 2.4
Freestream turbulence at reference conditions	Tu	= 0.8 %

Figure 1: **LRN-OGV cascade for wind tunnel tests (5 of 7 blades are shown) and design parameters and test conditions at ADP**

Test Facility and Measurement Techniques

The experiments were performed in the transonic cascade wind tunnel [19, 20] at DLR in Cologne. This wind tunnel is a closed loop, continuously running facility with a variable nozzle, an upper transonic wall, and a variable test section height. The air supply system enables an inlet Mach number range from 0.2 to 1.4 and a Mach number independent variation of the Reynolds number from 1x10^5 to 3x10^6. Figure 2 shows on the left hand side the cross section of the transonic cascade wind tunnel, where the measurement planes (MP 1 and MP 2), the lower and upper endwall suction as well as the main measured variables are illustrated. Furthermore, blade 4 is highlighted, because the wake measurements at midspan were performed behind this blade. Blade 3 and 5, were instrumented with static pressure taps at midspan on the pressure (blade 5) and suction side (blade 3) respectively. Additionally, the spanwise flow symmetry is verified by static pressure taps on both endwalls near the pressure and suction side, respectively.

Additionally, on the right hand side of Fig.2 the cascade parameters and the location of the measurement planes (MP 1 and MP 2) are depicted. For the tests the inlet total temperature was about

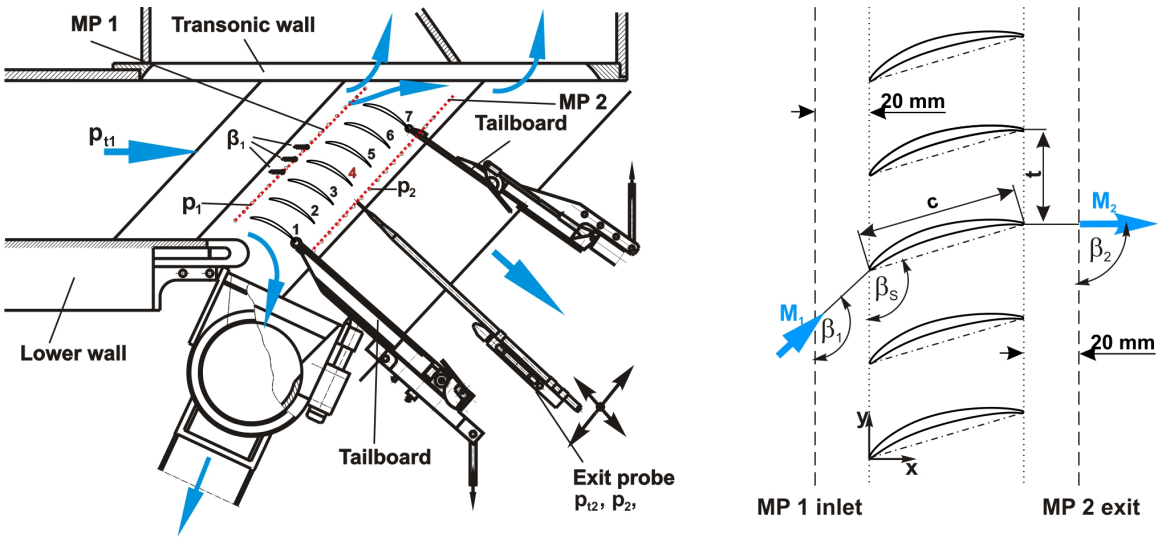

Figure 2: **Cross section of the DLR transonic cascade wind tunnel (left), cascade parameters and definition of measurement planes (right)**

Table 1: ESTIMATED UNCERTAINTIES OF THE TEST DATA AT MID-SPAN

Upstream flow angle	β_1	+/- 0.2 deg
Exit flow angle	β_2	+/- 0.2 deg
Mid-span loss coefficient	ω	+/- 0.002

300 K, the free stream turbulence level was around 0.8 percent. The test procedure included wake measurements with a combined 5-hole and 3-hole probe which are carried out at an inflow Mach number of 0.60, in order to identify the loss distribution in the wake behind the LRN-OGV cascade at measurement plane 2 (MP 2). To obtain the oil streak patterns on the blade and endwall surfaces a mixture of oil and titanium dioxide is used. The estimated uncertainties of the test data at midspan are presented in Table 1.

PIV Measurement Techniques

Tomo and Stereo PIV measurements are carried out near the suction side of a single passage in an area coincident with the numerically predicted location of the passage vortex. A detailed description of the measurement setup is given in [11]. Figure 3 shows a photograph of the tomographic PIV setup which involves four double-frame (PIV) cameras fitted with Scheimpflug mounts to account for the oblique imaging arrangement. Two cameras observe the volume of interest along the suction side at a pitch angle of zero while the other camera pair observes the measurement volume from above at 26 deg and 34 deg pitch angle in order to have a sufficient angular aperture of the system.

Both single-axis and two-axis Scheimpflug mounts are used to optimize the depth of focus of each camera. The f-numbers range from 8 to 16 in order to minimize optical distortions due to the oblique viewing through the Perspex window. The observed common field of view (FOV) has a size of approximately 36×24 mm and is located near the trailing edge of the blade. The thickness of the illuminated volume was successively adjusted to approximately 1 mm and 3.5 mm FWHM for stereo and tomographic PIV during each wind tunnel run. Volumetric image data was acquired in three regions at distances of 4, 8 and 11 mm with respect to the side wall in order to cover the entire corner

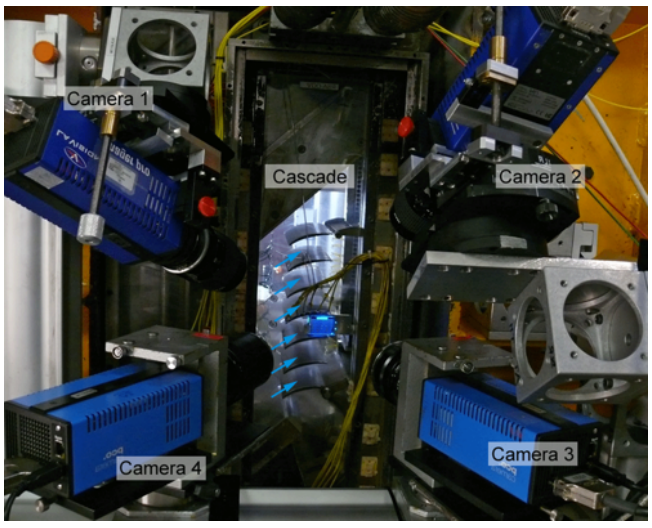

Figure 3: **Tomo PIV camera setup and back-illuminated calibration target on a micro traverse within the cascade**

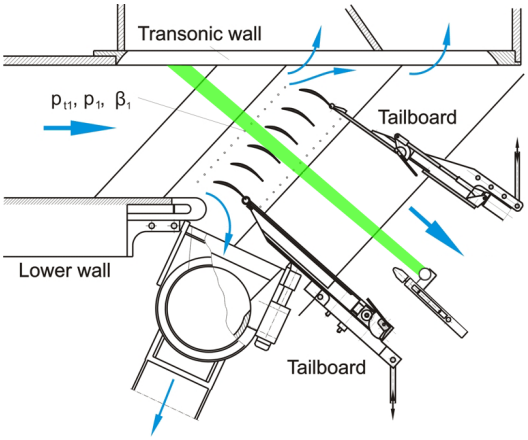

Figure 4: **The TGK test section and light-sheet orientation**

vortex. Each volume has a maximum size of $36\times24\times4$ mm^3. The velocities within each subvolume are additionally measured at three equally spaced planes using thin sheet stereo PIV and cameras no.1 and no.3 at a combined viewing angle of 50 deg.

The light sheet probe (see Fig. 4) is positioned 450 mm downstream of the trailing edge of the cascade. The beam enters the cascade through a 500 mm long, 16 mm diameter probe whose tip contains a 90 deg deflecting mirror. The probe is additionally supported from the inside of the tunnel in order to reduce aerodynamically induced bending and vibrations which would affect the light sheet position. Previously conducted PIV measurement campaigns showed that the tunnel flow carries significant amounts of rust particles whose high momentum can lead to a fast erosion of the reflective coating on the 90 deg turning mirror at the light-sheet probe's tip. To improve the protection of the mirror surface from incoming particles (rust) the probe tip was retrofitted with a Laval nozzle which redirects and accelerates the purge flow against the tunnel flow, ideally at supersonic speed [9]. Thereby incoming particles are sufficiently decelerated and prevent the erosion of mirror surface.

The cascade wind tunnel facility is seeded with an atomized paraffine-ethanol mixture (1:2) dispersed by two atomizers. An impactor and a dryer between atomizer and test section limited the maximum droplet diameter to approximately 1μm. In an effort of improving the global seeding homogeneity a seeding injection rake was installed on the screens within the settling chamber upstream of the test section. This ensured the distribution of the particles over a larger area compared to streamline seeding. A detailed response time evaluation of the applied seeding can be found in [9] and reports a shock response time of 0.77 μs based upon velocity profiles measured across a normal shock at $M_1 = 1.25$. The average response length corresponds to 0.23 μm.

Camera calibration and accuracy

The subvolumes are calibrated with a traversed micro target [10] which consists of back-illuminated calibration points at a spacing of 2 mm and a diameter of 0.4 mm. The lateral accuracy of point spacing is $\pm$ 0.3μm. Seven calibration planes at 1 mm z-spacing were recorded. The vendor of the micro traverse states a positioning accuracy in z of $\pm$ 2μm. The measured point correspondences of world and camera coordinates are used to fit mapping functions according to world-to-image and image-to-world projection. Global image shifts due to tunnel vibrations were monitored simultaneously with tomographic measurements and are on the order of $\approx$ 0.5 pixel for cameras no.3 and no.4 and of $\approx$ 1 pixel for camera no.1. By comparison, the sizes of particle images vary between 2-6 pixel depending on the camera view. Therefore these vibrations are not taken into account and neglected during the tomographic PIV evaluation.

Particle volume reconstruction and displacement recovery

Both conventional (stereo) PIV and tomographic PIV are very susceptible to laser flare, such as light reflected by the blades or scattered by slight scratches or seeding deposits on the windows. Therefore image data is first processed using background subtraction and spatial filtering to enhance overall contrast thereby improving the visibility of particle images.

Three dimensional reconstruction of the imaged particle volume is achieved with the maximum entropy reconstruction technique (MENT) [14]. Details of the MENT implementation are given in [11].

State-of-the-art cross-correlation processing is used for particle displacement recovery in both planar and volume PIV. Both algorithms employ a resolution pyramid which starts at a rather coarse grid and stepwise increases resolution while continually updating a predictor field [16, 17]. At a given resolution level integer-based sample offsetting is applied in a symmetric fashion using the estimate from the previous resolution step [22, 23]. Intermediate validation is based on normalized median filtering as proposed by Westerweel & Scarano [24]. Once the desired final spatial resolution

Table 2: **Evaluation parameters of stereo PIV and tomographic PIV**

	Stereo PIV (thin sheet)	Tomographic PIV (thick sheet)
field of view (FOV)	$\approx .36\times24$ mm^2	$\approx .36\times24$ mm^2
light sheet thickness	1.1 mm	3.5 mm
size of ROI	1800×1200 px at 50 px/mm	1800×1200×300 vx at 50 vx/mm
image enhancement	Subtraction of min. image 3x3 median filter 7x7 high pass filter 3x3 low-pass filter	Subtraction of min. image local minimum subtraction (5x5 kernel) normalization by avg. image intensity clipping
mapping algorithm	2nd order projection map and disparity correction	ratios of 2nd order polynomials
image interpolation	4th order B-Spline	bi-linear
reconstruction algorithm	-	MENT, 2 iterations
interrogation method	multi-resolution (3 levels) image deformation (3 passes)	3-D correlation, multi-resolution (3 levels) volume deformation (3 passes)
sub-pixel peak location	Whittaker reconstruction	3-point Gauss fit
interrogation window	64×48 px	64×32×32 vx
sampling grid	32×24 px	32×16×16 vx
validation	max.displacement diff. < 5 px normalized median filter (≤ 3)	normalized median filter (≤ 3) light sheet intensity > 50 %
final data grid	59×49 vectors	54×74×13 vectors

is reached image or volume deformation based on third-order B-splines [21] is applied at least twice to further improve the match between the image or volumes and thereby improving the displacement estimates.

The processing codes of both particle volume reconstruction and displacement recovery are highly parallelized to achieve optimal data throughput. The stereo PIV processing was done with PIVview 3.5 (PIVTEC GmbH, Germany). An overview of the involved processing steps is given in Tab. 2.

Numerical Approach

The numerical simulations were carried out using DLR's in-house flow solver for turbomachinery applications, TRACE [1]. TRACE solves the Favre-averaged Navier-Stokes equations using a density-based, compressible, hybrid-grid, finite volume method with an implicit time marching scheme. Statistical turbulence models are employed since scale resolving simulations are still far from being routinely applied in industrial environments due to time and cost restrictions. Linear eddy viscosity models such as the Menter SST k-ω model [13], possibly used in conjunction with ad hoc extensions modelling effects such as stream line curvature, are the industrial state of the art. While the deficiencies of a linear approach to turbulence modelling are well-known, the current study serves the purpose of assessing its predictive accuracy, also with the prospect to evaluate the potential of advanced, anisotropy-resolving approaches in future studies.

Especially in turbines but also in compressor configurations, laminar-to-turbulent transition plays an important role in the proper description of the flow. In this study, the predictive performance of the Menter SST k-ω model without ad hoc extensions coupled with the γ-Re$_\theta$ transition model by Langtry and Menter [12] is evaluated. While the γ-Re$_\theta$ approach does not model the physics of transition, it does provide a framework for the implementation of correlation-based methods. According

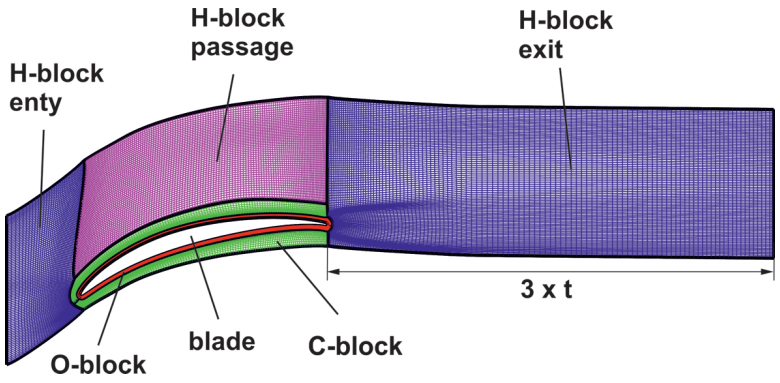

Figure 5: **Multi-block grid topology**

to its authors, the model is able to simulate all transition modes.

Half the spanwise extent of one blade passage was simulated, assuming nearly periodic conditions in pitchwise direction and a symmetry plane at mid-span. The numerical domain was discretised with a total number of 1.7 million cells in a multi-block structured mesh using an OCH-topology as shown in Fig. 5. 2D non-reflecting boundary conditions were employed at inflow and outflow boundaries. All boundary layers were resolved down to the viscous sublayer yielding an average y^+ of about 0.5, the growth ratio normal to the wall between the cells is below 1.2. Furthermore, a mesh study was performed in order to check the mesh dependency. Using the current mesh as a starting point, a coarser mesh was constructed by halving the number of points in streamwise an wall-normal direction; a finer mesh was generated by doubling the points in all directions. The results showed that there are no significant differences between the numerical results of the current and the fine mesh. For this reason, the original mesh was used for the current investigation.

RESULTS

Fig. 6 shows the secondary flow velocities obtained by averaging $N = 510$ individual PIV recordings. In order to show the chordwise vortex development, six orthogonal planes are extracted from nine stereo PIV planes. The color represents the v-w magnitude while the vectors show the in-plane

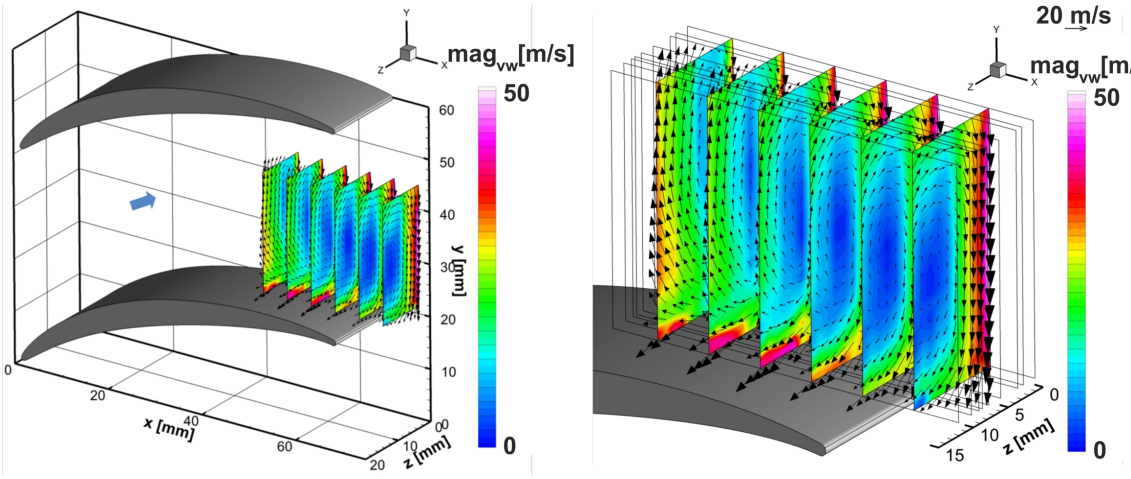

Figure 6: **Time averaged secondary flow velocities obtained from averaged stereo PIV measurements at 9 planes each with 1mm sheet thickness; overview (left) and detailed flow field and boundaries of the stereo PIV planes (right)**

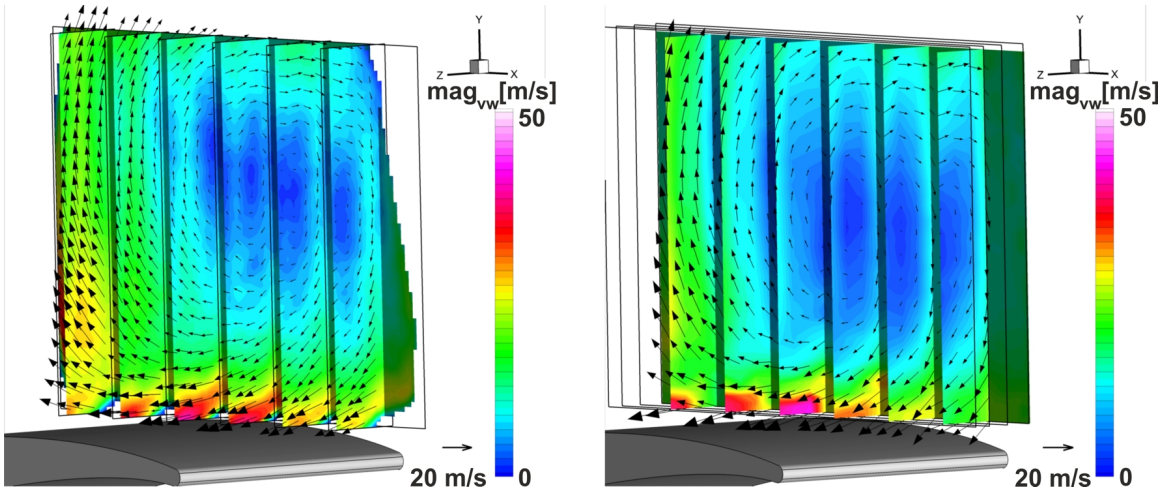

Figure 7: **Average of N = 500 tomographic measurements for a volume of 36 $\times$ 24 $\times$ 4 mm^3 at z = 8 mm distance from the endwall (left) and stereo PIV result (right) obtained by interpolation from three light sheet planes within the reconstructed domain. Every third vector along each dimension is plotted**

v-w velocity. Secondary flow velocities in between the stereo PIV planes are obtained by inverse distance interpolation. These results show the downstream development of the passage vortex.

Furthermore, Figure 7 (left) shows time-averaged velocities of one subvolume within a distance of 6 to 10 mm to the side wall in comparison to a stereo PIV result (right). Six secondary flow planes within the volume are plotted to show the passage vortex development. The colored contour represents v-w-magnitude, that is, the in-plane velocity. Regions outside the common intersection of all cameras are blanked as well as regions which have a light sheet intensity clearly below 50 %. Within each plane only the in-plane components of every third vector are plotted to enhance the visibility of the secondary flow which otherwise would be lost in the presence of the strong out-of-plane component (mean flow). The passage vortex can clearly be identified. The tomo PIV v-w magnitudes are a

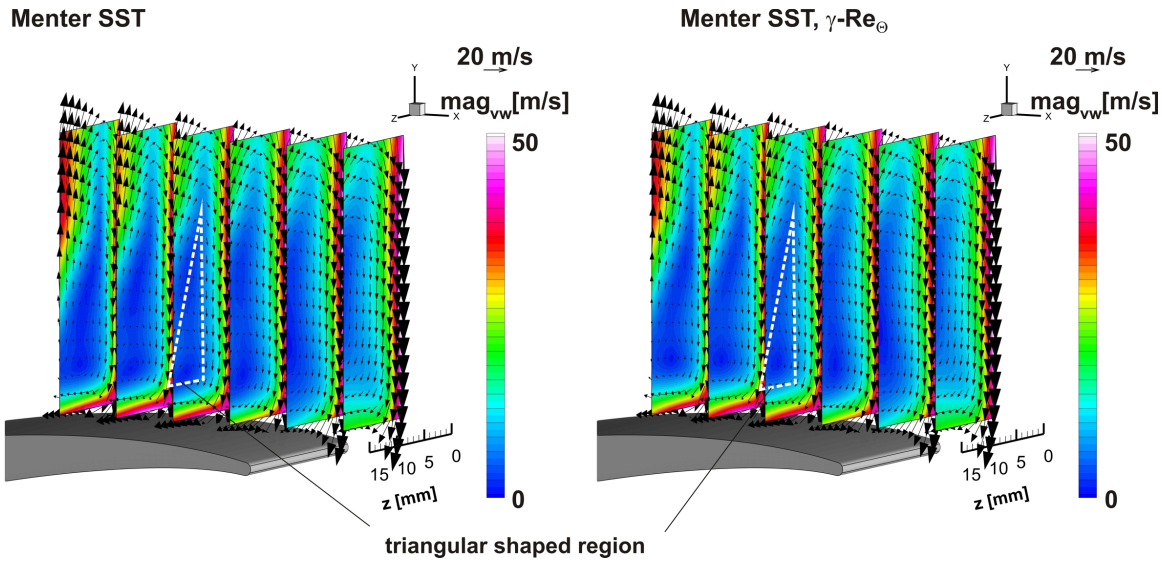

Figure 8: **Numeric results for the v-w magnitude and the in plane v-w velocity, Menter SST k-ω turbulence model (left), Menter SST k-ω turbulence model and γ-Re$_\theta$ transition model (right)**

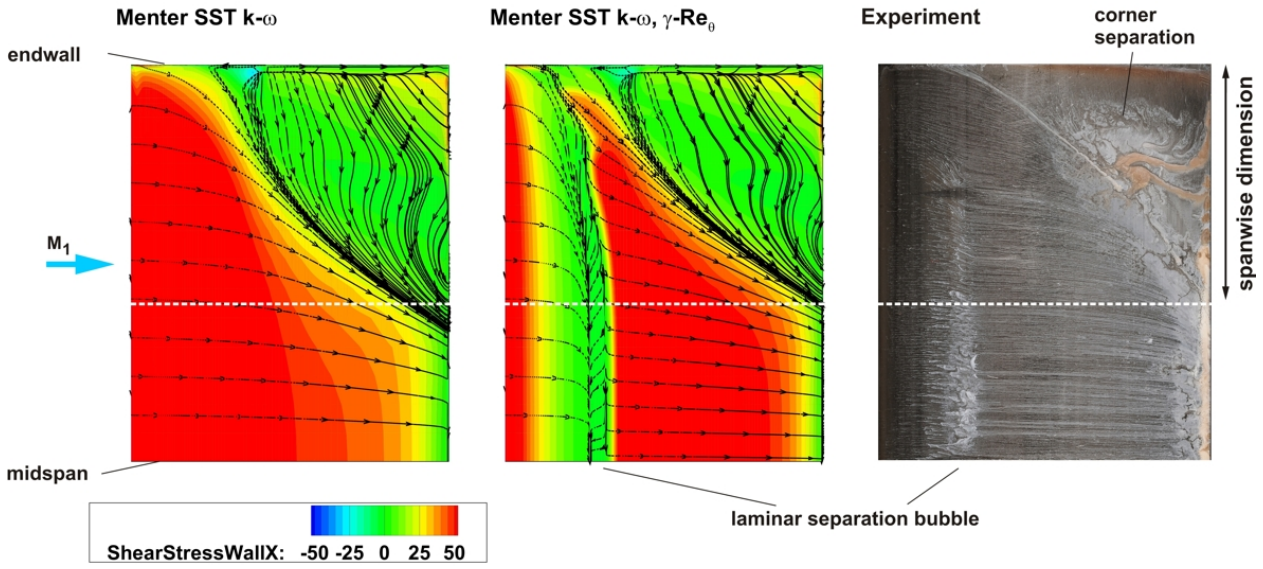

Figure 9: **Numerical streak lines, Menter SST k-ω turbulence model (left), Menter SST k-ω turbulence model and γ-Re$_\theta$ transition model (middle) and oil streak pattern on blade suction side (right)**

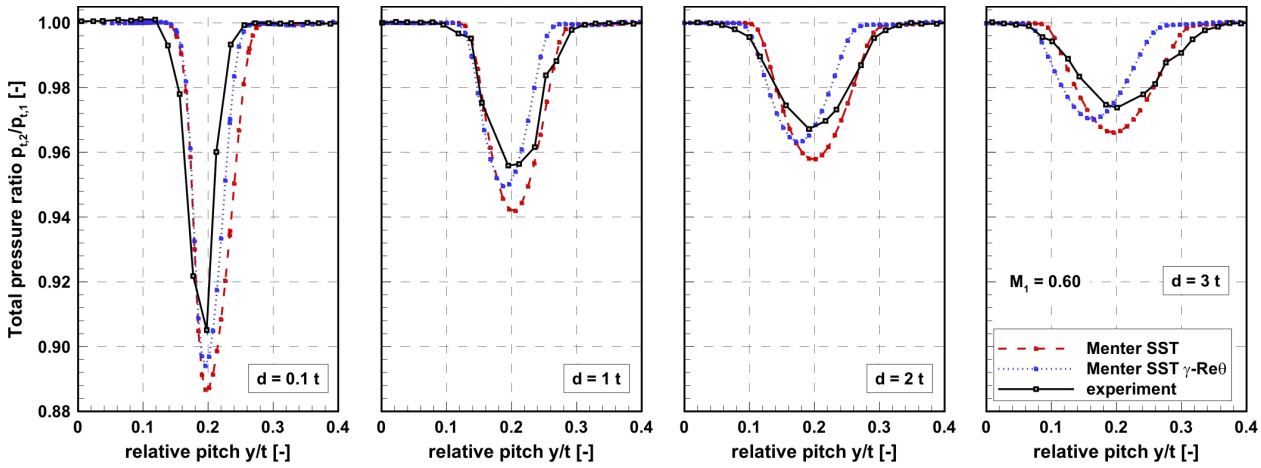

Figure 10: **Experimental and numerical results of the total pressure ratio wakes at midspan of the cascade, four distances d = 0.1t, 1t, 2t, 3t behind the cascade trailing are shown**

little bit lower than the stereo PIV results. The Figure shows that the secondary flow velocities near the blade suction side are larger for the tomographic PIV.

In contrast to that, the comparison of the numerical streak lines and experimental oil streak pattern in Fig. 9 depicts another behaviour. The correct flow topology including the laminar separation bubble can only be reproduced by the numerical setup with the coupled turbulence and transition model. The fully turbulent simulation overpredicts the secondary flow region in the corner because its dimension in spanwise direction is larger.

In comparison to the PIV results (Fig. 7) the numerical results are shown in Fig. 8. The color represents the v-w magnitude while the vectors show the in-plane v-w velocity. The numerical results show a large triangular shaped region (marked in Fig. 8) of low v-w magnitude and the corresponding velocity vectors. This is a typical behaviour of the simulated flow in the corner region of a compressor blade passage and it shows the deficiency of the linear eddy viscosity approach in Menters SST k-ω

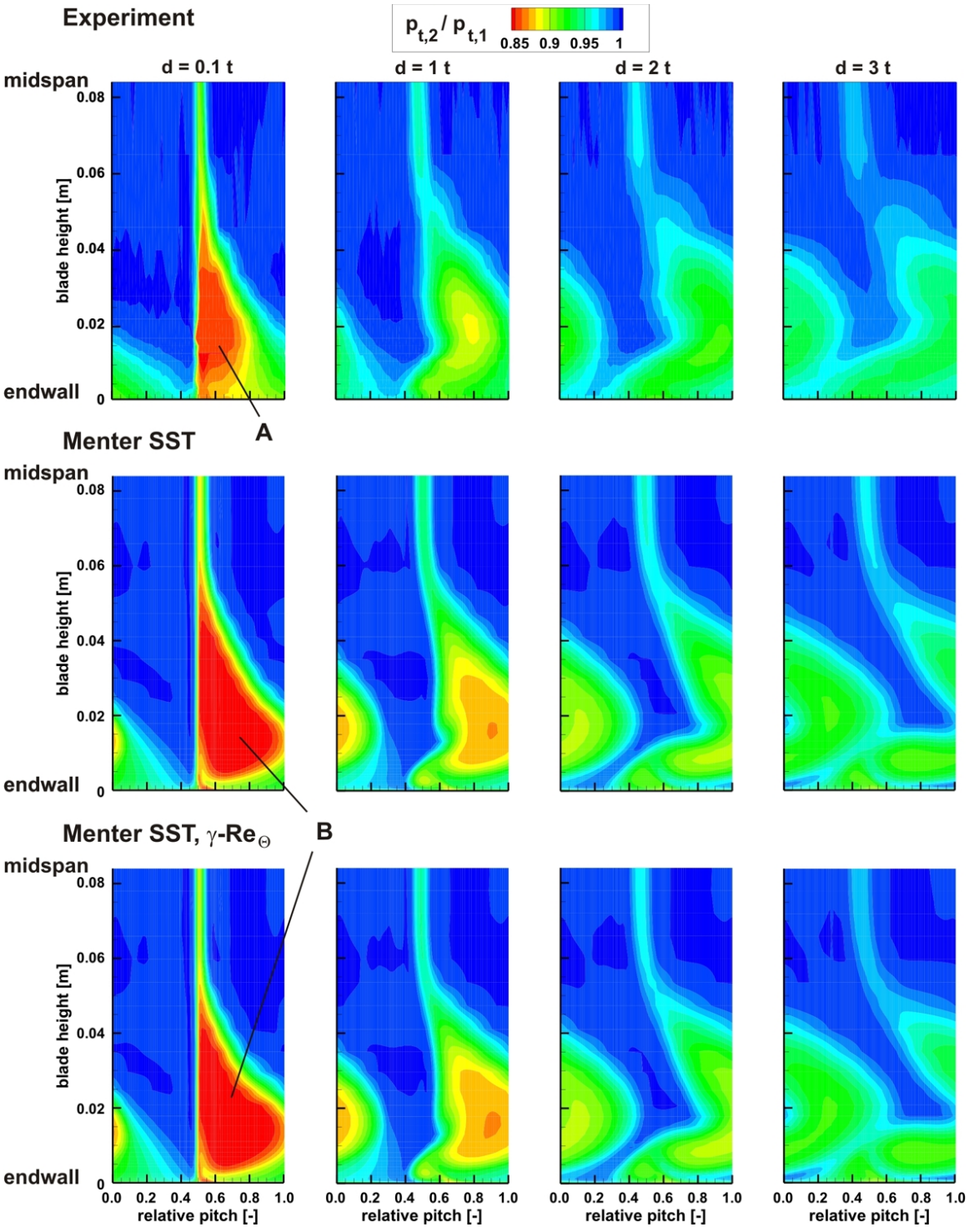

Figure 11: **Experimental and numerical 2D distributions of the total pressure ratio behind the cascade, four distances d = 0.1t, 1t, 2t, 3t from trailing are shown**

turbulence model in comparison to the PIV measurement results. It is indicated by these numerical results that the cascade losses will be overpredicted. In addition to that, there are no significant differences between the numerical results with and without transition model. From this point of view the usage of a transition model is not necessary in order to improve compressor simulations.

The influence of the transition model can also be seen in Figure 10. Concerning the profile losses, this figure illustrates the mixing behaviour between the wake and the mean flow downstream of the

cascade trailing edge at midspan. The position of the trailing edge is the same for the experimental and numerical results. It is shown that the mixing behaviour is well simulated, but the wake depth is overpredicted by the numerical results. The usage of the transition model improves the numerical results and brings it closer to the experimental ones. There is a pitchwise shift of the loss peak position between the numerical results observable. This shift increases with an increasing distance from the trailing edge. This behavior results from the different boundary layer development due to the used transition model and the resulting slight difference of the outflow angle. In comparison to that, the constant pitchwise position of the experimental wake results from the adjustment of the wake probe on the wake outflow angle.

In general it can be noticed, that for the simulation of compressors in turbomachinery transition can not be neglected. Therefore, the further development of turbulence and transition models is important, in order to achieve a more accurate prediction of working range limits.

Fig. 11 shows the numerical and experimental distributions of the total pressure ratio at four downstream positions behind the cascade trailing edge. This figure illustrates that in the plane close to the trailing edge (d = 0.1t) the high loss region in the numerical results (marked with B) is overpredicted compared to the experimental results marked with A. As already mentioned, the typical triangular shape of the high loss region at the numerical results is visible at the d = 0.1t position. Furthermore, the blade height extension of the loss region which is caused by secondary flow effects in the corner shows considerable differences between the numerical and experimental results. The mixing behaviour as well as the rotation of the loss region due to the passage vortex rotation from d = 0.1t to 3t are relatively well reproduced by the numerical simulation. Nevertheless, all numerical results show a overprediction of the loss intensity. However, the correct estimation of the losses is a crucial factor in the calculation of the compressor working range. Thus, an improved representation of turbulent effects is needed.

CONCLUSIONS

An experimental and numerical study of a subsonic compressor cascade was performed in order to provide extensive validation data by means of stereo PIV, advanced tomographic PIV as well as conventional wake measurements by a 3- and 5-hole probe. Within the study a comparison of the experimental results with the numerical results was carried out. The outcome of the study show that the flow and loss behaviour is well predicted in general by the numerical setup and used turbulence model. In addition to that, the results of the study show that transitional effects on the compressor blades are not negligible. The use of a transition model is recommended. In the next development stage, in order to achieve a more accurate prediction which is necessary for a more detailed simulation of the working range, advanced, anisotropy-resolving turbulence models have to be considered.

REFERENCES

[1] K. Becker, K. Heitkamp, and E. Kügeler. Recent Progress in a Hybrid-Grid CFD Solver for Turbomachinery Flows. Fifth European Conference on Computational Fluid Dynamics, ECOMAS CFD 2010, Lisbon, Portugal, June 14-17 2010.

[2] G. Elsinga, F. Scarano, B. Wieneke, and B. van Oudheusden. Tomographic particle image velocimetry. *Experiments in Fluids*, 41:933–947, 2006.

[3] S. A. Gbadebo, N. A. Cumpsty, and T. P. Hynes. Three-Dimensional Separations in Axial Compressors. *Journal of Turbomachinery, ASME*, 127(2):331–339, April 2005.

[4] A. Hergt, W. Hage, S. Grund, W. Steinert, M. Terhorst, F. Schongen, and Y. Wilke. Riblet Ap-

plication in Compressors: Towards efficient Blade Design? Number GT2014-25142 in ASME Turbo Expo, Düsseldorf, Germany, 16-20, June 2014.

[5] A. Hergt, R. Meyer, and K. Engel. Effects of Vortex Generator Application on the Performance of a Compressor Cascade. *ASME Journal of Turbomachinery*, 135(2):021027–1 – 021027–10, March 2013.

[6] A. Hergt, W. Steinert, and S. Grund. Design and Experimental Investigation of a Compressor Cascade for Low Reynolds Number Conditions. Number ISABE-2013-1104 in 21st ISABE Conference, Busan, Korea, 9-13 September 2013.

[7] J. H. Horlock and B. Lakshminarayana. Secondary Flow: Theory, Experiment, and Application in Turbomachinery Aerodynamics. *Annual Review of Fluid Mechanics*, 5:247–280, 1973.

[8] J. H. Horlock, J. F. Luis, P. M. E. Percival, and B. Lakshinarayana. Wall Stall in Compressor Cascades. *Journal of Basics Engineering, ASME*, pages 637–648, September 1966.

[9] J. Klinner, A. Hergt, M. Beversdorff, and C. Willert. Visualization and PIV Measurements of the Transonic Flow around the Leading Edge of an eroded Fan Airfoil. 16th Int Symp on Applications of Laser Techniques to Fluid Mechanics, Lisbon, Portugal, 09-12 July 2012.

[10] J. Klinner and C. Willert. Tomographic shadowgraphy for three-dimensional reconstruction of instantaneous spray distributions. *Experiments in Fluids*, 53:531–543, 2012.

[11] J. Klinner and C. Willert. Application of Tomographic PIV in a Transonic Cascade. In *10th International Symposium on Particle Image Velocimetry - (PIV13), Delft, Netherlands*, 2013.

[12] R. Langtry and F. Menter. Correlation-Based Transition Modeling for Unstructured Parallelized Computational Fluid Dynamics Codes. *AIAA J.*, 47(12):2894–2906, 2009.

[13] F. Menter, M. Kuntz, and R. Langtry. Ten years of Industrial experience with the SST model. In K. Hanjalić, Y. Nagano, and M. Tummers, editors, *Turbulence, Heat and Mass Transfer 4*, 2003.

[14] G. Minerbo. MENT: A Maximum Entropy Algorithm for Reconstructing a Source from Projection Data. *Graphics and Image Processing*, (10), 1979.

[15] A. K. Prasad. Stereoscopic particle image velocimetry. *Experiments in Fluids*, 29:103–116, 2000.

[16] M. Raffel, C. Willert, S. Wereley, and J. Kompenhans. *Particle Image Velocimetry, A Practical Guide*. Springer Berlin-Heidelberg, 2007.

[17] F Scarano. Iterative image deformation methods in PIV. *Measurement Science and Technology*, 13(1):R1, 2002.

[18] H. Schlichting and A. Das. Recent Research on Cascade-Flow Problems. *Journal of Basic Engineering, ASME*, pages 221–228, March 1966.

[19] H. A. Schreiber, H. Starken, and W. Steinert. Transonic and Supersonic Cascades. *AGARDOgraph "Advanced Methods for Cascade Testing"*, AGARD AG 328:35–59, 1993.

[20] W. Steinert, R. Fuchs, and H. Starken. Inlet Flow Angle Determination of Transonic Compressor Cascade. *ASME Journal of Turbomachinery*, 114(3):487–493, July 1992.

[21] P. Thévenaz, T. Blu, and M. Unser. Interpolation revisited. *IEEE Transactions on Medical Imaging*, 19(7):739–758, July 2000.

[22] S. T. Wereley and C. D. Meinhart. Second-order accurate particle image velocimetry. *Experiments in Fluids*, 31(3):258–268, 2001.

[23] J. Westerweel, D. Dabiri, and M. Gharib. The effect of a discrete window offset on the accuracy of cross-correlation analysis of digital PIV recordings. *Experiments in Fluids*, 23(1):20–28, 1997.

[24] J. Westerweel and F. Scarano. Universal outlier detection for PIV data. *Experiments in Fluids*, 39(6):1096–1100, 2005.